Dopant solubility and charge compensation in La-doped SrSnO₃ films

Cite as: Appl. Phys. Lett. **115**, 152103 (2019); https://doi.org/10.1063/1.5119272 Submitted: 09 July 2019 . Accepted: 19 September 2019 . Published Online: 08 October 2019

Tristan Truttmann, Abhinav Prakash 🗓, Jin Yue, Thomas E. Mates, and Bharat Jalan 🗓



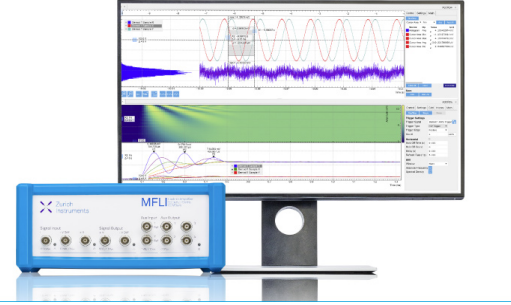














Dopant solubility and charge compensation in La-doped SrSnO₃ films

Cite as: Appl. Phys. Lett. **115**, 152103 (2019); doi: 10.1063/1.5119272 Submitted: 9 July 2019 · Accepted: 19 September 2019 · Published Online: 8 October 2019







Tristan Truttmann, 1,a) Abhinav Prakash, 1 🕞 Jin Yue, 1 Thomas E. Mates, 2 and Bharat Jalan 1,a)

AFFILIATIONS

- Department of Chemical Engineering and Materials Science, University of Minnesota, Minneapolis, Minnesota 55455, USA
- ²Materials Department, University of California, Santa Barbara, Santa Barbara, California 93106, USA

ABSTRACT

We investigate lanthanum (La) as an n-type dopant in the strain-stabilized tetragonal phase of SrSnO₃ grown on GdScO₃ (110) using a radical-based hybrid molecular beam epitaxy approach. Fully coherent, epitaxial films with an atomically smooth film surface were obtained irrespective of doping density. By combining secondary ion mass spectroscopy and Hall measurements, we demonstrate that each La atom contributes one free electron to the film, confirming that it occupies the Sr site in SrSnO₃ and that it is completely activated. Carrier density exceeding 1×10^{20} cm⁻³ was achieved in La-doped SrSnO₃ films, which is in excellent agreement with the dopant-solubility limit predicted by density functional theory calculations. A record-high room-temperature mobility of $70 \text{ cm}^2 \text{ V}^{-1} \text{ s}^{-1}$ at $1 \times 10^{20} \text{ cm}^{-3}$ was obtained in a 12 nm La-doped SrSnO₃ film, making this the thinnest perovskite oxide semiconductor with electron mobility exceeding $25 \text{ cm}^2 \text{ V}^{-1} \text{ s}^{-1}$ at room temperature. We discuss the structure-dopant-transport property relationships, providing essential knowledge for the design of electronic devices using these materials.

Published under license by AIP Publishing. https://doi.org/10.1063/1.5119272

Alkaline-earth stannates, in particular, cubic BaSnO₃ (BSO), have attracted significant attention for their wide bandgap and excellent dopability with reasonably high room-temperature electron mobilities reaching up to 320 cm² V⁻¹ s⁻¹ in bulk single crystals¹ and 183 cm² V⁻¹ s⁻¹ in thin films.² These high mobilities are attributed to low electron effective mass and weak electron-phonon scattering at room temperature.^{3,4} The mobility-limiting factor in BSO thin films is ascribed predominantly to the large threading dislocation density from the film/ substrate lattice mismatch.^{2,3,5,6} Insulating buffer layers have been used in an effort to reduce the density of threading dislocations, 2,3,6,7 but although they have resulted in moderate improvements in mobility, the lack of coherent films still stands between BSO and the goal of bulklike electronic transport. Some progress has been made in the synthesis of high-quality substrates with larger lattice parameters, but this effort is still at its infancy.⁸⁻¹¹ Likewise, homoepitaxial growth of BSO films has shown limited success with mobilities $\leq 100 \text{ cm}^2 \text{ V}^{-1} \text{ s}^{-1.12}$

SrSnO₃ (SSO) has many similarities to BSO including a wide bandgap (4.0–5.0 eV)^{13,14} and a low electron effective mass.¹⁵ Similar to BSO, the conduction band minimum in SSO is derived predominantly from Sn-5*s* states offering low electron effective mass.^{15–17} Bulk SSO has three noncubic polymorphs: an orthorhombic phase (*Pnma*) at room temperature, an orthorhombic phase with the *Imma* space group at

905 K < T < 1062 K, and a tetragonal phase (I4/mcm) at T > 1062 K before transitioning to a cubic structure at 1295 K. ¹⁸ Most significantly, coherent films of SSO have already been grown on commercially available substrates. ¹⁵ The tetragonal phase of SSO can also be stabilized at room temperature using epitaxial compressive strain, whereas an orthorhombic phase (Pnma) is achieved under tensile strain. ¹⁵ Significant progress has also been made with the fundamental understanding of the band structures, ^{15–17} optical properties, ^{13,16,19} carrier localization, ²⁰ electron–electron interaction, ²¹ electrostatic control, ²² and defect-driven magnetism. ^{19,23} Early device work using SSO as a channel material has yielded exciting results with the record-high peak transconductance value of 17 mS/mm in a depletion mode La-doped SSO (LSSO) n-channel metal–semiconductor field-effect transistor. ²⁴

There remain, however, several open questions including the optimal choice of dopant site and ion, dopant solubility, activation energy and the relative importance of the crystal structure, defects (ionized vs neutral), and electron-phonon scattering on electronic transport. Density functional theory calculations suggest lower formation energy of compensating acceptor defects in LSSO than in Ladoped BSO, limiting the maximum achievable electron density to $\sim \! 1 \times 10^{20} \, \mathrm{cm}^{-3}$ (i.e., La solubility limit) in LSSO, 25 but this is yet to be experimentally tested.

^{a)}Authors to whom correspondence should be addressed: trutt009@umn.edu and bjalan@umn.edu

Here, we report a systematic study of La-doping in the strain-stabilized tetragonal phase of SSO films grown on GdScO₃ (GSO) (110) by radical-based hybrid molecular beam epitaxy (MBE). We show that our experimental results are in reasonably good agreement with the calculated maximum achievable carrier density in LSSO prior to the onset of carrier compensation. Using high-resolution X-ray diffraction, secondary ion mass spectroscopy (SIMS), and Hall measurements, we demonstrate a one-to-one correspondence between the La-dopant concentration and the measured electron density in addition to establishing the structure-dopant-transport relationships in tetragonal-phase LSSO films.

LSSO films were grown on GSO (110) using a radical-based hybrid MBE approach.^{26,27} This approach employs a chemical precursor-hexamethylditin (HMDT)-for Sn, conventional solid sources for Sr and La (ultrahigh purity of >99.99%), and a radio frequency (RF) plasma source for oxygen. La was used as an n-type dopant. Films were grown using codeposition in an ultrahigh vacuum MBE chamber (EVO-50, Omicron) with a base pressure of 10⁻¹⁰ Torr. All films were grown at a substrate temperature of 900 °C (thermocouple temperature) and under a fixed oxygen pressure of 5×10^{-6} Torr supplied using a RF plasma source operating at 250 W. The La doping concentration was tuned by varying the temperature of the effusion cell, T_{La}, between 1180 and 1220 °C. Stoichiometry optimization and the details of the MBE method are described elsewhere. 15,20 Structural characterization was performed using a high-resolution Panalytical X'Pert thin film diffractometer with Cu K_{α} radiation. Wide-angle X-ray diffraction (WAXRD) 2θ - ω coupled scans were taken to determine phase purity and the out-of-plane lattice parameters. Film thicknesses were determined using the X-ray Kiessig fringes. Atomic force microscopy (AFM) was used for surface characterization. SIMS profiles were collected with a Cameca IMS 7f-Auto (Cameca, Gennevilliers, France). To calibrate SIMS for La quantification, the count ratios of ¹³⁹La: ¹¹²Sn were compared to a La-ion-implanted standard. The standard was implanted with $2 \times 10^{14} \, \text{cm}^{-2}$ La at 50 keV with an angle 7° away from perpendicular to the sample to avoid channeling. The La concentration in the films was analyzed with a 5 keV O2+ primary beam which was rastered across a $150 \times 150 \ \mu \text{m}^2$ sample area. An electron gun was used to minimize sample charging. Electronic transport measurements were performed in a Quantum Design Physical Property Measurement System (PPMS Dynacool) using a van der Pauw configuration to measure the sheet carrier density, sheet resistance, and carrier mobility. For Hall measurements, magnetic fields were swept between -9 T and +9 T. Indium was used as an Ohmic contact.

Figure 1 shows AFM images of 12 nm LSSO/2 nm SSO/GSO (110) as a function of $T_{\rm La}$, revealing atomically smooth film surfaces with root mean square (rms) roughness values between 115 and 314 pm. Figure 2(a) shows the high-resolution X-ray diffraction patterns of these films, indicating phase-pure, singe crystalline films with Kiessig fringes. The sample structure is illustrated in Fig. 2(c). The presence of Kiessig fringes reveals uniform films with excellent interface abruptness and smooth morphology. These results further reveal an expanded out-of-plane lattice parameter of 4.106 \pm 0.002 Å consistent with the strain-stabilized tetragonal SSO polymorph on GSO (110)¹⁵ irrespective of doping density. Figure 2(b) shows the corresponding rocking curves of these films, revealing narrow and broad Gaussian components for all doping levels as illustrated in the inset. The values of the full-width at half maximum (FWHM) vary between

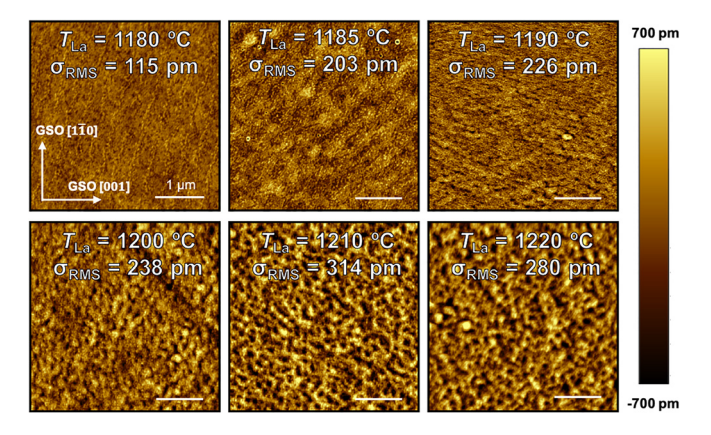


FIG. 1. AFM images as a function of $T_{\rm La}$ for 12 nm LSSO/2 nm SSO/GSO (110) films showing atomically smooth film surfaces.

 0.046° and 0.053° for the narrow component and 0.33° and 0.60° for the broad component. In comparison, the FWHM of the substrate rocking curves is nominally 0.016°, which is significantly narrower than either film component. The two-Gaussian shape is commonly seen in epitaxial films. The narrow component is ascribed to a longrange uncorrelated disorder limited by the substrate, whereas the broad component is attributed to the correlated short-range disorder.²² Generally, the broad component emerges in films after strain relaxation and has been associated with the disorder from the dislocation defects.²⁹ We note, however, that 14 nm SSO grown on GSO (110) is fully coherent, 15 and thus, the strain relaxation cannot be the cause for this correlated short-range disorder. These results, however, suggest the presence of short-range correlated structural disorder of unknown origin in these films, which may also depend on the doping concentration. Future studies should focus on understanding the microscopic origin of these disorders. To this end, as a measure of structural disorder, we define the intensity ratio of two Gaussian peaks, $I_{\rm broad}/I_{\rm narrow}$, as a "disorder proxy." Larger disorder proxy means a higher degree of short-range correlated structural disorder. Figure 2(d) shows the

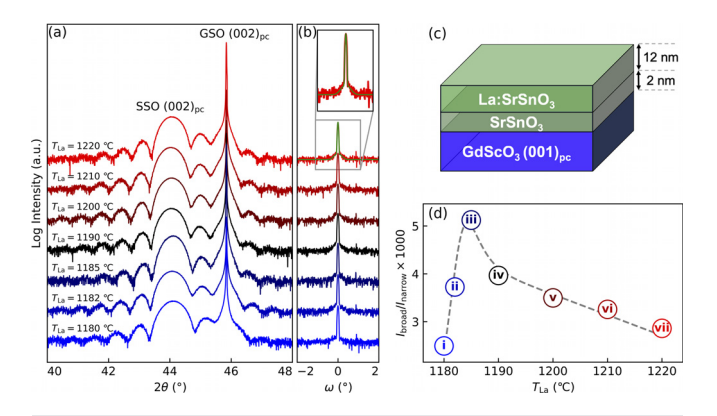


FIG. 2. (a) On-axis high-resolution X-ray diffraction scans and (b) the rocking curves around the (002) film peak of 12 nm LSSO/2 nm SSO/GSO (110) films as a function of T_{La} . (c) A schematic of the sample. The inset of part b shows narrow and broad components using a two-Gaussian fit. (d) The intensity ratio of broad and narrow peaks ($I_{\text{broad}}/I_{\text{narrow}}$) as a function of T_{La} .

disorder proxy as a function of $T_{\rm La}$, revealing that the disorder proxy first increases and then decreases with increasing $T_{\rm La}$. Experimental results are shown using circular symbols with a sample number embedded inside the symbol for convenient illustration of the data. To investigate the role of structural disorder in electrical transport, we correlate the disorder proxy with the electronic transport in the discussion that follows below.

Figure 3(a) shows the three-dimensional carrier densities at room temperature (n_{3D}) of 12 nm LSSO/2 nm SSO/GSO (110) as a function of $T_{\rm La}$. With the exception of sample (iii), with increasing $T_{\rm La}$, $n_{\rm 3D}$ increases expectedly, reaching a maximum value of $1.1 \times 10^{20} \, \text{cm}^$ followed by a decrease for $T_{\rm La} > 1210\,^{\circ}{\rm C}$, suggesting the La solid solubility limit in LSSO and the onset of carrier compensation.²⁵ No measurable conduction was observed in the films doped at $T_{\rm La} < 1180\,^{\circ}{\rm C}$ for $t \le 12$ nm. In contrast, however, thicker LSSO films with t > 12 nm showed significant conductivity even for lower T_{La} and the same growth rate. These results reflect the important role of surface depletion (see Fig. S1). We, therefore, note that the reported $n_{\rm 3D}$ in this study, which is determined by dividing the measured 2D carrier density by the film thickness of 12 nm, is likely smaller than the actual dopant density in the film. This interpretation is consistent with our findings from thicker LSSO films [48 nm LSSO/2 nmSSO/GSO (110)] doped at $T_{\text{La}} = 1150 \,^{\circ}\text{C}$, which resulted in $n_{\text{3D}} = 7.5 \times 10^{19} \, \text{cm}^{-3}$. This density is higher than the value obtained at $T_{\rm La} = 1180\,^{\circ}{\rm C}$ in 12 nm LSSO films, confirming significant carrier depletion in thinner films. To get further insights into the doping dependence of the depletion width, we show in Fig. S1 the calculated depletion width as a function of doping level for a range of surface built-in potentials. For instance, at $N_d=8\times 10^{19}\,\text{cm}^{-3}$, the depletion width can vary between 2 and 8 nm. If the film thickness is 48 nm, the depletion width only constitutes about 5%-15% of the overall thickness, and therefore, the influence on the measured hall density is not significant as compared

To further investigate whether or not the dopant atoms are fully activated, we performed a SIMS depth-profile measurement on 48 nm

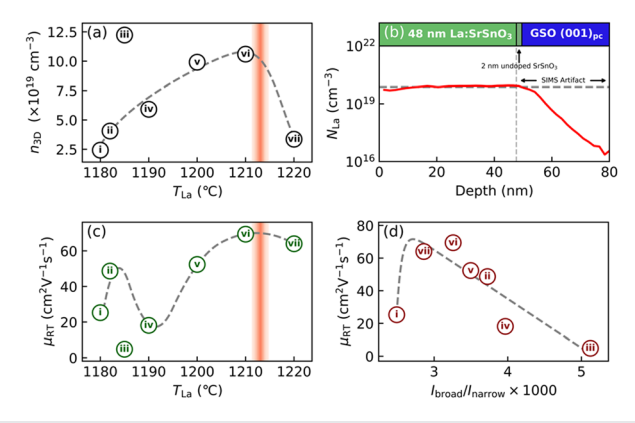


FIG. 3. (a) $n_{\rm 3D}$ as a function of $T_{\rm La}$ for 12 nm LSSO/2 nm SSO/GSO (110) and (b) SIMS depth-profile showing the La-dopant concentration ($N_{\rm La}$) as a function of depth of 48 nm LSSO/2 nm SSO/GSO (110). The horizontal dashed line marks the position corresponding to the measured $n_{\rm 3D}$ from Hall measurements, indicating one-to-one correspondence with $N_{\rm La}$. [(c) and (d)] $\mu_{\rm RT}$ as a function of $T_{\rm La}$ and $I_{\rm broad}/I_{\rm narrow}$, respectively, for 12 nm LSSO/2 nm SSO/GSO (110). The vertical line in parts (a) and (c) marks the onset of charge compensation.

LSSO/2 nm SSO/GSO (110), doped at $T_{\rm La}=1150\,^{\circ}{\rm C}$. The La concentration was quantified using the SIMS calibration standard. Figure 3(b) shows an excellent one-to-one correspondence between the La concentration (red bold line) and the measured $n_{\rm 3D}$ (marked by the horizontal dashed line), demonstrating fully activated dopants in LSSO films. This result further reveals no measurable surface depletion effect in 48 nm LSSO/2 nm SSO/GSO (110) at the given doping density. It is noted that a small discrepancy between the La-dopant concentration and the $n_{\rm 3D}$ near the film surface (over \sim 10 nm) and a sharp decay (about 7 nm/decade) of the La-signal at the SSO/GSO interface are known SIMS artifacts.

Figure 3(c) shows the room-temperature mobility (μ_{RT}) of these samples as a function of $T_{\rm La}$. With increasing $T_{\rm La}$, $\mu_{\rm RT}$ first increases and then decreases followed by an increase for 1185 $^{\circ}$ C $\leq T_{\rm La} \leq$ 1210 $^{\circ}$ C reaching a maximum value of $70 \text{ cm}^2 \text{ V}^{-1} \text{ s}^{-1}$ at $1.1 \times 10^{20} \text{ cm}^{-3}$. For $T_{\rm La}$ > 1210 $^{\circ}$ C as marked by a vertical shaded line, $\mu_{\rm RT}$ decreases moderately, suggesting increased scattering. The moderate decrease in mobility above 1210°C is likely related to the solubility limit illustrated in Fig. 3(a) through either the creation of defects or the loss of carrier screening from the drop in the carrier concentration. However, the increase in mobility with increasing La density for 1185 $^{\circ}$ C $\leq T_{La} \leq$ 1210 $^{\circ}$ C is surprising. A similar behavior has been seen in compensated semiconductors and is attributed to the charged-impurity scattering. For instance, in relaxed La-doped BSO films, such a behavior is ascribed to scattering by charged dislocations.^{3,30} In this context, the observed behavior in LSSO films is surprising, given these films are fully coherent, 15 and may also suggest that the source of these disorders is charged. However, since the disorder proxy decreases with increasing doping, it is difficult to comment on the charge-state of the source of these disorders. To this end, we plotted μ_{RT} as a function of the disorder proxy in Fig. 3(d), revealing a notable dependence of mobility on disorder proxy. It was also found that the lowest doped sample (labeled "i") despite having the lowest disorder proxy resulted in lower mobility. These results suggest that roomtemperature mobility of LSSO films in the measured doping density range is largely limited by the structural disorder. However, the origin of these structural disorders and their doping dependence is yet to be understood and will be a subject of future study.

In summary, we have investigated La-doping in the tetragonal phase of SSO, revealing a strong correlation between doping density and structural disorder. The room-temperature carrier mobility of $70\,\mathrm{cm^2~V^{-1}\,s^{-1}}$ at $1.1\times10^{20}\,\mathrm{cm^{-3}}$ was obtained in 12 nm LSSO films. A carrier density exceeding $1\times10^{20}\,\mathrm{cm^{-3}}$ was observed prior to the onset of carrier compensation, suggesting the La solubility limit of the order of $10^{20}\,\mathrm{cm^{-3}}$ in the tetragonal phase of SSO grown on GSO (110). Using SIMS and the Hall measurements, we show that the La concentration matches one-to-one with the measured $n_{3\mathrm{D}}$, suggesting fully activated La dopant atoms. At low doping, surface depletion becomes important and accounts for the loss of conductivity in thin films. Future work should focus on exploring the doping dependence of structural disorder as well as on investigating the origin of surface depletion.

See the supplementary material for the calculation of depletion widths as a function of dopant concentration in La-doped SSO films.

This work was supported through the Young Investigator Program of the Air Force Office of Scientific Research (AFOSR) through Grant Nos. FA9550-16-1-0205 and FA9550-19-1-0245. Part of this work was supported by the National Science Foundation through DMR-1741801 and partially by the UMN MRSEC program under Award No. DMR-1420013. Parts of this work were carried out in the Characterization Facility, University of Minnesota, which receives partial support from NSF through the MRSEC program. We also acknowledge partial support from the renewable development funds (RDF) of the Institute on the Environment (UMN) and the Norwegian Centennial Chair Program seed funds.

REFERENCES

- ¹H. J. Kim, U. Kim, H. M. Kim, T. H. Kim, H. S. Mun, B.-G. Jeon, K. T. Hong, W.-J. Lee, C. Ju, K. H. Kim, and K. Char, Appl. Phys. Express 5(6), 061102 (2012)
- ²H. Paik, Z. Chen, E. Lochocki, H. Ariel Seidner, A. Verma, N. Tanen, J. Park, M. Uchida, S. L. Shang, B.-C. Zhou, M. Brützam, R. Uecker, Z.-K. Liu, D. Jena, K. M. Shen, D. A. Muller, and D. G. Schlom, APL Mater. 5(11), 116107 (2017).
- ³A. Prakash, P. Xu, A. Faghaninia, S. Shukla, J. W. Ager III, C. S. Lo, and B. Jalan, Nat. Commun. 8, 15167 (2017).
- ⁴K. Krishnaswamy, B. Himmetoglu, Y. Kang, A. Janotti, and C. G. Van de Walle, Phys. Rev. B **95**(20), 205202 (2017).
- ⁵W.-J. Lee, H. J. Kim, J. Kang, D. H. Jang, T. H. Kim, J. H. Lee, and K. H. Kim, Annu. Rev. Mater. Res. 47, 391 (2017).
- ⁶S. Raghavan, T. Schumann, H. Kim, J. Y. Zhang, T. A. Cain, and S. Stemmer, APL Mater. **4**(1), 016106 (2016).
- ⁷A. P. N. Tchiomo, W. Braun, B. P. Doyle, W. Sigle, P. van Aken, J. Mannhart, and P. Ngabonziza, APL Mater. 7, 041119 (2019).
- ⁸R. Uecker, R. Bertram, M. Brutzam, Z. Galazka, T. M. Gesing, C. Guguschev, D. Klimm, M. Klupsch, A. Kwasniewski, and D. G. Schlom, J. Cryst. Growth 457, 137 (2017).
- ⁹D. H. Jang, W.-J. Lee, E. Sohn, H. J. Kim, D. Seo, J.-Y. Park, E. J. Choi, and K. H. Kim, J. Appl. Phys. **121**, 125109 (2017).
- ¹⁰D. Souptel, G. Behr, and A. M. Balbashov, J. Cryst. Growth 236, 583 (2002).

- ¹¹C. Xin, P. Veber, M. Guennou, C. Toulouse, N. Valle, M. C. Hatnean, G. Balakrishnan, R. Haumont, R. S. Martin, M. Velazquez, A. Maillard, D. Rytz, M. Josse, M. Maglione, and J. Kreisel, CrystEngComm 21, 502 (2019).
- ¹²W.-J. Lee, H. J. Kim, E. Sohn, T. H. Kim, J.-Y. Park, W. Park, H. Jeong, T. Lee, J. H. Kim, K.-Y. Choi, and K. H. Kim, Appl. Phys. Lett. 108, 082105 (2016).
- ¹³T. Schumann, S. Raghavan, K. Ahadi, H. Kim, and S. Stemmer, J. Vac. Sci. Technol. A 34, 050601 (2016).
- ¹⁴E. Baba, D. Kan, Y. Yamada, M. Haruta, H. Kurata, Y. Kanemitsu, and Y. Shimakawa, J. Phys. D: Appl. Phys. 48, 455106 (2015).
- ¹⁵T. Wang, A. Prakash, Y. Dong, T. Truttmann, A. Bucsek, R. James, D. D. Fong, J.-W. Kim, P. J. Ryan, H. Zhou, T. Birol, and B. Jalan, ACS Appl. Mater. Interfaces 10, 43802 (2018).
- ¹⁶D. J. Singh, Q. Xu, and K. P. Ong, Appl. Phys. Lett. **104**(1), 011910 (2014).
- ¹⁷K. P. Ong, X. Fan, A. Subedi, M. B. Sullivan, and D. J. Singh, APL Mater. 3, 062505 (2015).
- ¹⁸M. Glerup, K. S. Knight, and F. W. Poulsen, Mater. Res. Bull. **40**(3), 507 (2005).
- ¹⁹D. Gao, X. Gao, Y. Wu, T. Zhang, J. Yang, and X. Li, Physica E **109**, 101 (2019).
- 20T. Wang, L. R. Thoutam, A. Prakash, W. Nunn, G. Haugstad, and B. Jalan, Phys. Rev. Mater. 1(6), 061601 (2017).
- ²¹Y. Jin, L. R. Thoutam, A. Prakash, T. Wang, and B. Jalan, Appl. Phys. Lett. 115, 082102 (2019).
- ²²L. R. Thoutam, J. Yue, A. Prakash, T. Wang, K. E. Elangovan, and B. Jalan, ACS Appl. Mater. Interfaces 11, 7666 (2019).
- ²³Q. Gao, H. L. Chen, K. F. Li, and Q. Z. Liu, ACS Appl. Mater. Interfaces 11, 18051 (2019).
- ²⁴V. R. S. K. Chaganti, A. Prakash, J. Yue, B. Jalan, and S. J. Koester, IEEE Electron Device Lett. 39(9), 1381 (2018).
- 25 L. Weston, L. Bjaalie, K. Krishnaswamy, and C. G. Van de Walle, Phys. Rev. B 97(5), 054112 (2018).
- 26A. Prakash, J. Dewey, H. Yun, J. S. Jeong, K. Andre Mkhoyan, and B. Jalan, J. Vac. Sci. Technol. A 33(6), 060608 (2015).
- ²⁷A. Prakash, P. Xu, X. Wu, G. Haugstad, X. Wang, and B. Jalan, J. Mater. Chem. C 5(23), 5730 (2017).
- ²⁸P. F. Miceli and C. J. Palmstrom, Phys. Rev. B **51**, 5506 (1995).
- ²⁹T. Wang, K. Ganguly, P. Marshal, P. Xu, and B. Jalan, Appl. Phys. Lett. 103, 212004 (2013)
- ³⁰H. Mun, U. Kim, H. Min Kim, C. Park, T. Hoon Kim, H. Joon Kim, K. Hoon Kim, and K. Char, Appl. Phys. Lett. **102**, 252105 (2013).